Date of publication xxxx 00, 0000, date of current version xxxx 00, 0000.

Digital Object Identifier

Adaptive Fault Detection for Grid-Forming Inverters

GABRIEL INTRIAGO[1], (Student Member, IEEE) and YU ZHANG[1], (Member, IEEE)
[1]Department of Electrical and Computer Engineering, University of California Santa Cruz, Santa Cruz, CA 95064 USA (e-mail: {gintriag,zhangy}@ucsc.edu)

Corresponding author: Yu Zhang (e-mail: zhangy@ucsc.edu)

This work was supported in part by a Seed Fund Award from The Center for Information Technology Research in the Interest of Society (CITRIS); in part by the Banatao Institute at the University of California; and in part by the Hellman Fellowship.

ABSTRACT This work introduces a residual-based adaptive threshold for detecting faults in grid-forming inverters in AC microgrids islanded from the main grid. The inverters are modeled as a nonlinear system with one-sided Lipschitz nonlinearities and modeling uncertainties. The adaptive threshold response is evaluated using unwanted events such as busbar and sensor faults. An inequality for the upper bound on the ℓ_2 norm of the residual is derived and used for designing the adaptive threshold. The upper bound is obtained via semidefinite programming with two linear matrix inequality constraints. In the numerical tests, we consider an islanded-mode AC microgrid with two grid-forming inverters, one grid-following inverter, and one synchronous machine with the governor and excitation control. Primary and secondary control layers regulate the operation of the inverters in the microgrid. The performance of our proposed adaptive threshold clearly edges over a fixed threshold method.

INDEX TERMS Microgrids, grid-forming inverters, adaptive threshold, fault detection.

Nomenclature

α_{i}	Rotating angle of the i-th inverter
$\gamma_{\mathrm{di,qi}}$	d-axis and q-axis auxiliary state variables for the PI current controllers at the i-th inverter
ω_{b}	Nominal frequency of the microgrid
ω_{ci}	Cut-off frequency of the low-pass filters for the active and reactive power at the i-th inverter
ω_{i}	Frequency of the i-th inverter
ω_{ni}	Nominal frequency of the i-th inverter
ω_{r}	Frequency of the common reference frame
$\phi_{\mathrm{di,qi}}$	d-axis and q-axis auxiliary state variables for the PI voltage controllers at the i-th inverter
$\mathrm{C_{fi}}$	Capacitance of the LC filter at the i-th inverter
$\mathrm{i_{bdi,bqi}}$	d-axis and q-axis current magnitude of the i-th branch
$\mathrm{i_{ldi,lqi}}$	d-axis and q-axis output current magnitude of the i-th inverter
$\mathrm{i^{*}_{ldi,lqi}}$	d-axis and q-axis output current magnitude of the PI voltage controller at the i-th inverter
$\mathrm{i_{lodi,loqi}}$	d-axis and q-axis current magnitude of the i-th load
$\mathrm{i_{odi,oqi}}$	d-axis and q-axis current magnitude of the LC filter at the i-th inverter
$\mathrm{K_{IC_i}}$	Current PI controller's integral gain at the i-th inverter
$\mathrm{K_{IV_i}}$	Voltage PI controller's integral gain at the i-th inverter
$\mathrm{K_{PC_i}}$	Current PI controller's proportional gain at the i-th inverter
$\mathrm{K_{PV_i}}$	Voltage PI controller's proportional gain at the i-th inverter
$\mathrm{L_{br}}$	Inductance of the i-th branch
$\mathrm{L_{ci}}$	Output connector's inductance at the i-th inverter
$\mathrm{L_{fi}}$	Inductance of the LC filter at the i-th inverter
$\mathrm{L_{lo}}$	Inductance of the i-th load
$\mathrm{m_{Pi}}$	Active power droop coefficient at the i-th inverter
$\mathrm{n_{Qi}}$	Reactive power droop coefficient at the i-th inverter
$\mathrm{P_i}$	Active power of the i-th inverter
$\mathrm{Q_i}$	Reactive power of the i-th inverter
$\mathrm{R_{br}}$	Resistance of the i-th branch
$\mathrm{R_{ci}}$	Output connector's resistance at the i-th inverter

R_{fi} Resistance of the LC filter at the i-th inverter
R_{lo} Resistance of the i-th load
$v_{bdi,bqi}$ d-axis and q-axis bus voltage magnitude at the PCC of the i-th inverter
v_{bi} Total bus voltage magnitude $\sqrt{v_{bdi}^2 + v_{bqi}^2}$ of the i-th inverter
$v_{idi,iqi}^*$ d-axis and q-axis output voltage magnitude of the PI current controller at the i-th inverter
V_{ni} Nominal voltage magnitude of the i-th inverter
$v_{odi,oqi}$ d-axis and q-axis output voltage magnitude of the i-th inverter
$v_{odi,oqi}^*$ d-axis and q-axis voltage magnitude references for the PI voltage controller at the i-th reference frame
v_{oi} Total output voltage magnitude $\sqrt{v_{bdi}^2 + v_{bqi}^2}$ of the i-th inverter

I. INTRODUCTION

Distributed energy resources (DERs) with power electronics-based interfaces are evolving from grid-following (GFL) to grid-forming inverters (GFM). GFMs will be an essential asset for future microgrids because they form the grid and offer better control at different timescales. The GFMs provide voltage and frequency support to the microgrid by resembling the role of a synchronous generator (SG) but with a clean energy source. The most important feature of GFMs is their embedded cascaded controller that establishes the grid's reference voltage and frequency in grid-connected and islanded modes. However, undesirable internal events, such as busbar or sensor faults, can lead to an unstable operation of the grid-forming inverters, affecting the system's overall stability. Threshold-based fault detection is a workhorse in practice. In a naive way, a designer can set a constant threshold to determine the presence of a fault. However, a constant threshold may lead to misdetection if its value is too high or false alarms if it is too low. Moreover, islanded microgrids are considered independent systems that must ensure the supply-demand power balance while providing voltage and frequency support. The operation of an islanded microgrid is more challenging than that of a grid-connected microgrid regarding stability. To cope with these challenges, this paper focuses on finding an adaptive threshold for grid-forming inverters operating in an islanded-mode AC microgrid.

A. PRIOR WORK

In general, fault detection algorithms for power converters can be categorized as data-driven, signal-processing, and model-based techniques. Data-driven techniques rely on various system measurements to extract fault signatures, thereby implementing fault diagnosis with intelligent algorithms [1]–[7]. In [1], the authors combine the information change in SCADA data with a recurrent neural network (RNN) to compute a residual and adaptive threshold for fault detection in inverters for wind turbines. In [2], a new spatio-temporal multiscale neural network provides an end-to-end fault diagnosis for wind turbines using imbalanced SCADA data. The approach uses multiple thresholding to isolate faults. The authors in [3] design a fixed threshold and a novel fault diagnostic method for three-phase multilevel converters using 2-D convolutional neural networks and a window-based feature extraction technique. Another approach presented in [4] combines a short-time wavelet entropy calculation method with long short-term memory networks (LSTM) and support vector machines (SVM) for fault detection in multilevel converters. In [5], the authors propose a convolutional neural network (CNN) for fault diagnosis of open-circuit failure in three-phase inverters with multiple thresholds. Despite the merits of these works, data-driven models usually suffer from issues such as high computational burden, low interpretability, complicated weights initialization, and sensitivity to input data.

Signal processing based methods generally sample voltage, current, and auxiliary signals without an accurate system model [8]–[12]. In [8], the authors propose a detection method based on topology symmetry analysis in healthy and faulty conditions for two-level three-phase pulse-width modulating rectifiers. Although the method is low-cost, robust, and uses a fixed threshold, the method has poor rapidity and requires significant tuning effort. The zero current in each phase current is combined with different features to detect open-circuit transistor faults in a type three-level rectifier, as referred to in [9]. However, the proposed method uses fixed thresholding and is specific to the inverter's type. The authors in [10] propose an improved diagnosis method for open-circuit faults using a fixed threshold and AC current distortion characteristics for voltage source rectifiers. In [11], the authors propose a detection method of calculating the mismatch among current paths using solely existing current measurements. The authors in [12] present an open-circuit fault detection method by using fixed thresholding and checking the arm voltage magnitude errors with no additional transducers or measurements. However, the method inevitably delays five control cycles to detect the faults.

Model-based methods are appropriate when the systems under study can be modeled accurately and allow interoperability with existing control layers [13]–[19]. In [13], the authors propose an adaptive fast voltage-based detection method for open-switch faults with an adaptive threshold. However, the method is sensitive to noise in measured currents. A detection method with an adaptive threshold is designed for open-circuit faults using a phase voltage vector residual [14]. Nonetheless, the approach has a narrow diagnosis time. The authors in [15] use a combination of a current observer, filter circuits, and an adaptive threshold to detect open-switch

faults of voltage source inverters. In [16], high-fidelity model-based detection and isolation filters are employed for open-circuit and current sensor faults. However, the method is sensitive to communication latency. References [17], [18] leverage H_-/H_∞ optimization to design fault detection filters with fixed thresholds for busbar and line faults for inverter-based resources. The methods, however, are limited to system-level solutions that do not scale. In [20], the authors present a model-based method for designing adaptive thresholds for fault detection. However, the designed threshold is limited to linear systems, has a narrow adaptive operation, and does not consider the control input for its computation. The authors in [21] propose a superimposed phase-current scheme with a voltage restraint element to detect faults in an islanded microgrid with grid-forming inverters. Although the method correctly identifies faults, the speed of detection is considerable.

From the review of the prior works, an internal fault detection solution for grid-forming inverters operating in islanded AC microgrids that is robust against disturbances and exhibits a fast detection response is still missing. To fill this gap, we develop a model- and residual-based fault detection threshold that evolves according to the input dynamics of the grid-forming inverter and requires no additional sensors. First, we derive the mathematical model of the grid-forming inverter considering the state space framework. The model considers external disturbances and parametric uncertainties. Based on the inverter model, we select a nonlinear $\mathcal{H}_\infty/\mathcal{H}_-$ observer to compute the discrepancy between the output of the grid-forming inverter and the model's output. Then, a reliable adaptive threshold is obtained by solving a semi-definite program with linear matrix inequalities. Finally, we study the performance of our design considering a busbar and sensor fault with modeling errors, nonlinear loads, and input delays.

B. CONTRIBUTIONS

Protecting grid-forming inverters against internal faults is essential for improving islanded AC microgrids' transient stability and operation. The low inertia characteristic of the inverters makes fault currents increase at high rates. Such a situation demands fast fault detection and clearance of a few milliseconds. Otherwise, severe and permanent harm may occur to the inverter and microgrid components. The novel contributions of our work are summarized as follows:

1) To the best of the authors' knowledge, this is the first attempt to propose an adaptive threshold for detecting faults in grid-forming inverters. The adaptive threshold is evaluated in an AC microgrid with a technology mix to show the practical merits of our method.
2) The proposed method exhibits fast fault detection and clearance response times, minimizing to zero the false alarm and missed detection rates for the faults considered in this study.
3) The threshold design shows considerable sensitivity to the studied faults and excellent robustness against disturbances and parametric uncertainties.
4) The proposed design is reliable under the effects of modeling errors, nonlinear loads, and input delays.

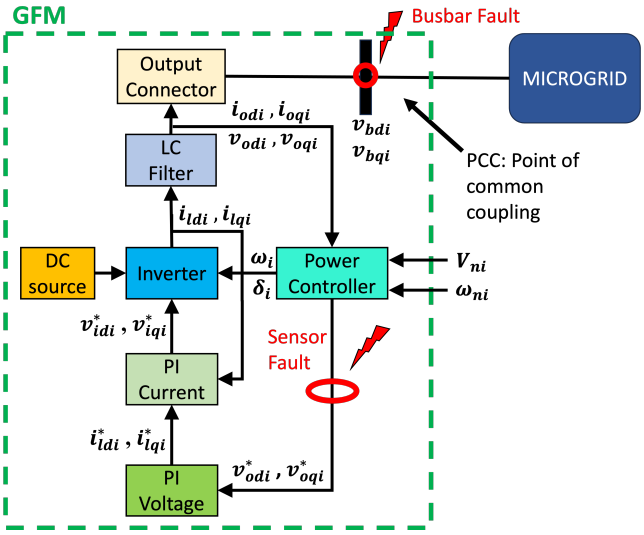

FIGURE 1: Block diagram of grid-forming inverter [22].

C. NOTATION AND ORGANIZATION

$\mathbb{R}$ is the set of real numbers. Vectors are represented by bold letters. $\mathbf{a}^\top$ is the transpose of vector $\mathbf{a}$. $\|\mathbf{a}\|$ represents Euclidean vector norm. $\langle \mathbf{a}, \mathbf{b} \rangle$ denotes the inner product of vectors $\mathbf{a}$ and $\mathbf{b}$. $\mathrm{A} \succ 0$ ($\mathrm{A} \prec 0$) means that matrix A is positive (negative) definite. The symbol $\times$ represents the Cartesian product. A zero matrix of appropriate dimensions is expressed as $\mathbf{0}$. $\mathrm{A_i}$ is the i-th column of matrix A.

The organization of this manuscript is presented as follows. Section II presents the modeling of the grid-forming inverter. Section III introduces the mathematical representation of nonlinear systems, the fault detection scheme, and the proposed adaptive threshold approach. The simulations and discussion are presented in Sections IV and V, respectively. The conclusions and final remarks are presented in Section VI.

II. GFM MODELING

The grid-forming inverter model considered in this work is described in the block diagram shown in Fig. 1. We assume that the GFMs are connected to a stable DC source. The voltage, current, and power controllers are tuned such that the GFM can form the microgrid's reference voltage magnitude and frequency. The power controller sets the operating frequency ($\omega_\mathrm{i} = \omega_\mathrm{ni} - \mathrm{m_{P_i}P_i}$) of the inverter bridge, provides the voltage magnitude

references ($v^*_{odi} = V_{ni} - n_{Q_i} Q_i, v^*_{oqi} = 0$) to the voltage controller, and contains the droop curves for power-sharing coordination. Using a PI control strategy, the voltage controller aligns the output voltage magnitude perpendicular to the q-axis and provides the current references to the current controller. The current controller uses a PI control strategy to charge/discharge the capacitor of the LC filter such that the desired voltage magnitude is achieved. Both PI controllers introduce auxiliary variables to simplify the state space modeling where $\dot{\phi}_{qi} = v^*_{oqi} - v_{oqi}$, $\dot{\phi}_{di} = v^*_{odi} - v_{odi}$, $\dot{\gamma}_{qi} = i^*_{lqi} - i_{lqi}$, and $\dot{\gamma}_{di} = i^*_{ldi} - i_{ldi}$. The output connector smoothens the output current of the GFM and couples it with the microgrid at the point of common coupling (PCC) [22], [23].

The dq frame of one of the microgrid's generators is selected as the common reference frame rotating at the frequency ω_r. Under ambient conditions, the rotating frame of the microgrid's power injection technologies overlaps the common reference frame. However, when a disturbance occurs, the disturbance introduces a phase difference $\delta_i = \int \omega_i - \omega_r$ between the power injection technologies and the reference generator where ω_i is the rotation frequency of each technology's frame. Consequently, the frame of each technology no longer overlaps with the common reference frame. According to [24], a rotation matrix is used to map the reference frame to the frame of each technology as follows

$$\begin{bmatrix} x_{bdi} \\ x_{bqi} \end{bmatrix} = \begin{bmatrix} \cos(\delta_i) & \sin(\delta_i) \\ -\sin(\delta_i) & \cos(\delta_i) \end{bmatrix} \begin{bmatrix} x_{bDi} \\ x_{bQi} \end{bmatrix}, \tag{1}$$

where x represents voltage (v) or current (i) magnitude. For example, the voltage magnitude at the point of common coupling, denoted as v_{bDi} and v_{bQi}, is converted to the frame of the i-th GFM as $v_{bdi} = \cos(\delta_i)v_{bDi} + \sin(\delta_i)v_{bQi}$, and $v_{bqi} = -\sin(\delta_i)v_{bDi} + \cos(\delta_i)v_{bQi}$. A similar conversion is applied for the current magnitude in the dq domain.

The ideal model of each GFM in the absence of faults and disturbances can be expressed in the following state-space form

$$\begin{cases} \dot{\mathbf{x}} = A\mathbf{x} + B\mathbf{u} + \boldsymbol{\phi}(\mathbf{x}, \mathbf{u}) \\ \mathbf{y} = C\mathbf{x} + D\mathbf{u}, \end{cases} \tag{2}$$

where $\mathbf{y} \in \mathbb{R}^{n_y}$ is the measurements vector, $\mathbf{x} \in \mathbb{R}^{n_x}$ is the state vector, $\mathbf{u} \in \mathbb{R}^{n_u}$ is the input vector, defined as

$$\mathbf{y} = [v^*_{odi}],$$
$$\mathbf{x} = [\delta_i \ P_i \ Q_i \ \phi_{di} \ \phi_{qi} \ \gamma_{di} \ \gamma_{qi} \ i_{ldi} \ i_{lqi} \ v_{odi} \ v_{oqi} \ i_{odi} \ i_{oqi}]^\top,$$
$$\mathbf{u} = [\omega_r \ \omega_{ni} \ V_{ni} \ v_{bdi} \ v_{bqi}]^\top.$$

The state space is formed by collecting and manipulating the equations (1)-(20) from [23]. The nonlinear function and state space matrices are shown in (3). The dynamic equations that govern the GFM state space representation are given in the Appendix. Moreover, the GFMs incorporate a distributed secondary control layer for the voltage magnitude and frequency. The objective of the secondary voltage controller is to set the input V_{ni} such that the voltage magnitude components converge to $v_{oqi} \to 0$ and $v_{odi} \to v_{ref}$. Similarly, the secondary frequency controller chooses the input ω_{ni} such that ω_i reaches ω_r. The distributed secondary control layer details can be found in [22].

III. METHODOLOGY

This section presents the residual generation, evaluation, and adaptive threshold design. The ideal state-space model of a nonlinear system subject to faults can be presented as follows

$$\begin{cases} \dot{\mathbf{x}} = A\mathbf{x} + B\mathbf{u} + \boldsymbol{\phi}(\mathbf{x}, \mathbf{u}) + E_f\mathbf{f} \\ \mathbf{y} = C\mathbf{x} + D\mathbf{u} + F_f\mathbf{f}, \end{cases} \tag{4}$$

where the terms $E_f\mathbf{f}$ and $F_f\mathbf{f}$ exist during the fault occurrence. E_f, F_f, and $\mathbf{f}$ are formed by appropriately manipulating and reorganizing the dynamic equations and the state-space matrices.

A. STATE-SPACE REPRESENTATION FOR NONLINEAR SYSTEMS

The state space model of a nonlinear dynamical system with parametric uncertainties can be expressed as follows

$$\begin{cases} \dot{\mathbf{x}} &= \bar{A}\mathbf{x} + \bar{B}\mathbf{u} + \bar{E}_w\mathbf{w} + E_f\mathbf{f} + \boldsymbol{\phi}(\mathbf{x}, \mathbf{u}) \\ \mathbf{y} &= \bar{C}\mathbf{x} + \bar{D}\mathbf{u} + \bar{F}_w\mathbf{w} + F_f\mathbf{f} \end{cases}, \tag{5}$$

where,

$$\begin{cases} \bar{A} = A + \Delta A & \bar{B} = B + \Delta B \\ \bar{C} = C + \Delta C & \bar{D} = D + \Delta D \\ \bar{E}_w = E_w + \Delta E_w & \bar{F}_w = F_w + \Delta F_w \end{cases},$$

and $\boldsymbol{\phi}(\mathbf{x}, \mathbf{u})$ captures the nonlinearities in the system. $\mathbf{f}$ is the vector of faults, and $\mathbf{w}$ is the vector of disturbances. The model's matrices are obtained based on the system's dynamical equations. E_f and F_f are the matrix representation of faults, while E_w and F_w correspond to the matrix representation of disturbances. The model uncertainties ΔA, ΔB, ΔC, ΔD, ΔE_w, and ΔF_w belong to the polytope defined as

$$\begin{bmatrix} \Delta A & \Delta B & \Delta E_w \\ \Delta C & \Delta D & \Delta F_w \end{bmatrix} = \mathrm{Co}\{\Xi_1, \ldots, \Xi_p\}, \tag{6}$$

$$\Xi_i = \begin{bmatrix} A_i & B_i & E_{wi} \\ C_i & D_i & F_{wi} \end{bmatrix}, \quad \forall i = 1, \ldots, p, \tag{7}$$

where Co denotes the convex hull. A_i, B_i, C_i, D_i, E_{wi}, and F_{wi}, $\forall i = 1, \ldots, p$ are known matrices of appropriate dimensions. The region of bounded operation of the system is defined as the Cartesian products of the convex sets $\mathcal{U}$ and $\mathcal{D}$. Each set is formed by the Cartesian product of the system's states' and inputs' maximum and minimum values [25]. The sets are defined

$$
\begin{cases}
\mathrm{A}^{\top} = \begin{bmatrix}
0 & 0 & 0 & 0 & 0 & 0 & 0 & 0 & 0 & 0 & 0 & 0 & 0 \\
-\mathrm{m_{P_i}} & -\omega_{\mathrm{ci}} & 0 & 0 & 0 & 0 & 0 & 0 & 0 & 0 & 0 & 0 & 0 \\
0 & 0 & -\omega_{\mathrm{ci}} & -\mathrm{n_{Q_i}} & 0 & -\mathrm{K_{PV_i}}\mathrm{n_{Q_i}} & 0 & -\frac{1}{\mathrm{L_{fi}}}\mathrm{K_{PC_i}}\mathrm{K_{PV_i}}\mathrm{n_{Q_i}} & 0 & 0 & 0 & 0 & 0 \\
0 & 0 & 0 & 0 & 0 & \mathrm{K_{IV_i}} & 0 & \frac{1}{\mathrm{L_{fi}}}\mathrm{K_{PC_i}}\mathrm{K_{IV_i}} & 0 & 0 & 0 & 0 & 0 \\
0 & 0 & 0 & 0 & 0 & 0 & \mathrm{K_{IV_i}} & 0 & \frac{1}{\mathrm{L_{fi}}}\mathrm{K_{PC_i}}\mathrm{K_{IV_i}} & 0 & 0 & 0 & 0 \\
0 & 0 & 0 & 0 & 0 & 0 & 0 & \frac{1}{\mathrm{L_{fi}}}\mathrm{K_{IC_i}} & 0 & 0 & 0 & 0 & 0 \\
0 & 0 & 0 & 0 & 0 & 0 & 0 & 0 & \frac{1}{\mathrm{L_{fi}}}\mathrm{K_{IC_i}} & 0 & 0 & 0 & 0 \\
0 & 0 & 0 & 0 & 0 & -1 & 0 & -\left(\frac{\mathrm{R_{fi}}}{\mathrm{L_{fi}}} + \frac{1}{\mathrm{L_{fi}}}\mathrm{K_{PC_i}}\right) & \omega_{\mathrm{b}} & \frac{1}{\mathrm{C_{fi}}} & 0 & 0 & 0 \\
0 & 0 & 0 & 0 & 0 & 0 & -1 & -\omega_{\mathrm{b}} & -\left(\frac{\mathrm{R_{fi}}}{\mathrm{L_{fi}}} + \frac{1}{\mathrm{L_{fi}}}\mathrm{K_{PC_i}}\right) & 0 & \frac{1}{\mathrm{C_{fi}}} & 0 & 0 \\
0 & 0 & 0 & -1 & 0 & -\mathrm{K_{PV_i}} & \omega_{\mathrm{b}}\mathrm{C_{fi}} & -\frac{1}{\mathrm{L_{fi}}} + \frac{1}{\mathrm{L_{fi}}}\mathrm{K_{PC_i}}\mathrm{K_{PV_i}} & \frac{1}{\mathrm{L_{fi}}}\mathrm{K_{PC_i}}\omega_{\mathrm{b}}\mathrm{C_{fi}} & 0 & 0 & \frac{1}{\mathrm{L_{ci}}} & 0 \\
0 & 0 & 0 & 0 & -1 & -\omega_{\mathrm{b}}\mathrm{C_{fi}} & -\mathrm{K_{PV_i}} & -\frac{1}{\mathrm{L_{fi}}}\mathrm{K_{PC_i}}\omega_{\mathrm{b}}\mathrm{C_{fi}} & -\left(\frac{1}{\mathrm{L_{fi}}} + \frac{1}{\mathrm{L_{fi}}}\mathrm{K_{PC_i}}\mathrm{K_{PV_i}}\right) & 0 & 0 & 0 & \frac{1}{\mathrm{L_{ci}}} \\
0 & 0 & 0 & 0 & 0 & \mathrm{F_i} & 0 & \frac{1}{\mathrm{L_{fi}}}\mathrm{K_{PC_i}}\mathrm{F_i} & 0 & -\frac{1}{\mathrm{C_{fi}}} & 0 & -\frac{\mathrm{R_{ci}}}{\mathrm{L_{ci}}} & 0 \\
0 & 0 & 0 & 0 & 0 & 0 & \mathrm{F_i} & 0 & \frac{1}{\mathrm{L_{fi}}}\mathrm{K_{PC_i}}\mathrm{F_i} & 0 & -\frac{1}{\mathrm{C_{fi}}} & 0 & -\frac{\mathrm{R_{ci}}}{\mathrm{L_{ci}}}
\end{bmatrix}, \\
\mathrm{B} = \begin{bmatrix}
-1 & 1 & 0 & 0 & 0 \\
0 & 0 & 0 & 0 & 0 \\
0 & 0 & 0 & 0 & 0 \\
0 & 0 & 1 & 0 & 0 \\
0 & 0 & 0 & 0 & 0 \\
0 & 0 & \mathrm{K_{PV_i}} & 0 & 0 \\
0 & 0 & 0 & 0 & 0 \\
0 & 0 & \frac{1}{\mathrm{L_{fi}}}\mathrm{K_{PC_i}}\mathrm{K_{PV_i}} & 0 & 0 \\
0 & 0 & 0 & 0 & 0 \\
0 & 0 & 0 & 0 & 0 \\
0 & 0 & 0 & 0 & 0 \\
0 & 0 & 0 & 0 & 0 \\
0 & 0 & 0 & -\frac{1}{\mathrm{L_{ci}}} & 0 \\
0 & 0 & 0 & 0 & -\frac{1}{\mathrm{L_{ci}}}
\end{bmatrix}, \quad \mathrm{C}^{\top} = \begin{bmatrix}
0 \\ 0 \\ -\mathrm{n_{Q_i}} \\ 0 \\ 0 \\ 0 \\ 0 \\ 0 \\ 0 \\ 0 \\ 0 \\ 0 \\ 0
\end{bmatrix}, \quad \mathrm{D}^{\top} = \begin{bmatrix}
0 \\ 0 \\ 1 \\ 0 \\ 0
\end{bmatrix}, \quad \boldsymbol{\phi}(\mathbf{x},\mathbf{u}) = \begin{bmatrix}
0 \\
\omega_{\mathrm{ci}}(\mathrm{v_{odi}}\mathrm{i_{odi}} + \mathrm{v_{oqi}}\mathrm{i_{oqi}}) \\
\omega_{\mathrm{ci}}(\mathrm{v_{oqi}}\mathrm{i_{odi}} - \mathrm{v_{odi}}\mathrm{i_{oqi}}) \\
0 \\ 0 \\ 0 \\ 0 \\
\omega_{\mathrm{ni}}\mathrm{i_{lqi}} - \mathrm{m_{P_i}}\mathrm{P_i}\mathrm{i_{lqi}} \\
-\omega_{\mathrm{ni}}\mathrm{i_{ldi}} + \mathrm{m_{P_i}}\mathrm{P_i}\mathrm{i_{ldi}} \\
\omega_{\mathrm{ni}}\mathrm{v_{oqi}} - \mathrm{m_{P_i}}\mathrm{P_i}\mathrm{v_{oqi}} \\
-\omega_{\mathrm{ni}}\mathrm{v_{odi}} + \mathrm{m_{P_i}}\mathrm{P_i}\mathrm{v_{odi}} \\
\omega_{\mathrm{ni}}\mathrm{i_{oqi}} - \mathrm{m_{P_i}}\mathrm{P_i}\mathrm{i_{oqi}} \\
-\omega_{\mathrm{ni}}\mathrm{i_{odi}} + \mathrm{m_{P_i}}\mathrm{P_i}\mathrm{i_{odi}}
\end{bmatrix}
\end{cases}, \tag{3}
$$

as $\mathcal{U} = [\mathrm{u_1^{min}}, \mathrm{u_1^{max}}] \times \cdots \times [\mathrm{u_p^{min}}, \mathrm{u_p^{max}}]$, and $\mathcal{D} = [\mathrm{x_1^{min}}, \mathrm{x_1^{max}}] \times \cdots \times [\mathrm{x_n^{min}}, \mathrm{x_n^{max}}]$.

A Luenberger observer for the dynamical model (5) can be posed as follows

$$
\begin{cases}
\dot{\hat{\mathbf{x}}} &= \mathrm{A}\hat{\mathbf{x}} + \mathrm{B}\mathbf{u} + \mathrm{L}(\mathbf{y} - \hat{\mathbf{y}}) + \phi(\hat{\mathbf{x}}, \mathbf{u}) \\
\hat{\mathbf{y}} &= \mathrm{C}\hat{\mathbf{x}} + \mathrm{D}\mathbf{u}
\end{cases}, \tag{8}
$$

where $\hat{\mathbf{y}}$ and $\hat{\mathbf{x}}$ represent the vector of estimated measurements and states respectively. L corresponds to the matrix gain of the observer. We assume the following two conditions hold true

1) The system is observable.
2) The signals $\mathbf{w}$ and $\mathbf{f}$ are finite and square-integrable in $\mathcal{L}_2$.

Remark 1. The design of an observer robust against disturbances is not the aim of this work. Hence, the observer matrix gain L is obtained following the principles presented in [26], [27] while considering the nonlinearities of the grid-forming inverters as one-sided Lipschitz continuous (refer to Appendix), enabling a less restrictive design [28].

B. GENERATION OF THE RESIDUAL

Let us define the measurement error $\mathbf{r} = \mathbf{y} - \hat{\mathbf{y}}$ and state error $\mathbf{e} = \mathbf{x} - \hat{\mathbf{x}}$. Define $\Phi \triangleq \phi(\mathbf{x}, \mathbf{u}) - \phi(\hat{\mathbf{x}}, \mathbf{u})$ and $\phi \triangleq \phi(\hat{\mathbf{x}}, \mathbf{u})$. Then, the dynamics of the state error can be characterized as

$$
\begin{cases}
\dot{\mathbf{e}} &= (\mathrm{A} - \mathrm{LC})\,\mathbf{e} + \left(\bar{\mathrm{E}}_{\mathrm{w}} - \mathrm{L}\bar{\mathrm{F}}_{\mathrm{w}}\right)\mathbf{w} + (\mathrm{E_f} - \mathrm{LF_f})\,\mathbf{f} \\
&\quad + \Phi + (\Delta\mathrm{A} - \mathrm{L}\Delta\mathrm{C})\,\mathbf{x} + (\Delta\mathrm{B} - \mathrm{L}\Delta\mathrm{D})\,\mathbf{u} \\
\mathbf{r} &= \mathrm{C}\mathbf{e} + \bar{\mathrm{F}}_{\mathrm{w}}\mathbf{w} + \mathrm{F_f}\mathbf{f} + \Delta\mathrm{C}\mathbf{x} + \Delta\mathrm{D}\mathbf{u}.
\end{cases} \tag{9}
$$

Let us rewrite the error dynamics as

$$
\begin{bmatrix} \dot{\mathbf{e}} \\ \dot{\mathbf{x}} \end{bmatrix} = \begin{bmatrix} \mathrm{A} - \mathrm{LC} & \Delta\mathrm{A} - \mathrm{L}\Delta\mathrm{C} \\ 0 & \mathrm{A} + \Delta\mathrm{A} \end{bmatrix} \begin{bmatrix} \mathbf{e} \\ \mathbf{x} \end{bmatrix} + \begin{bmatrix} \Delta\mathrm{B} - \mathrm{L}\Delta\mathrm{D} \\ \mathrm{B} + \Delta\mathrm{B} \end{bmatrix} \mathbf{u} + \begin{bmatrix} \bar{\mathrm{E}}_{\mathrm{w}} - \mathrm{L}\bar{\mathrm{F}}_{\mathrm{w}} \\ \bar{\mathrm{E}}_{\mathrm{w}} \end{bmatrix} \mathbf{w} + \begin{bmatrix} \mathrm{E_f} - \mathrm{LF_f} \\ \mathrm{E_f} \end{bmatrix} \mathbf{f} + \begin{bmatrix} \Phi \\ \phi \end{bmatrix},
$$

$$
\mathbf{r} = \begin{bmatrix} \mathrm{C} & \Delta\mathrm{C} \end{bmatrix} \begin{bmatrix} \mathbf{e} \\ \mathbf{x} \end{bmatrix} + \begin{bmatrix} \Delta\mathrm{D} \end{bmatrix} \begin{bmatrix} \mathbf{u} \end{bmatrix} + \begin{bmatrix} \bar{\mathrm{F}}_{\mathrm{w}} \end{bmatrix} \begin{bmatrix} \mathbf{w} \end{bmatrix} + \begin{bmatrix} \mathrm{F_f} \end{bmatrix} \begin{bmatrix} \mathbf{f} \end{bmatrix}.
$$

Also, let us define

$$
\tilde{\mathbf{e}} = \begin{bmatrix} \mathbf{e} \\ \mathbf{x} \end{bmatrix}, \quad \tilde{\mathbf{w}} = \mathbf{w}, \quad \tilde{\mathbf{u}} = \mathbf{u},
$$

$$
\widetilde{\mathrm{A}} = \begin{bmatrix} \mathrm{A} - \mathrm{LC} & \Delta\mathrm{A} - \mathrm{L}\Delta\mathrm{C} \\ 0 & \mathrm{A} + \Delta\mathrm{A} \end{bmatrix}, \quad \widetilde{\mathrm{B}} = \begin{bmatrix} \Delta\mathrm{B} - \mathrm{L}\Delta\mathrm{D} \\ \mathrm{B} + \Delta\mathrm{B} \end{bmatrix},
$$

$$
\widetilde{\mathrm{C}} = \begin{bmatrix} \mathrm{C} & \Delta\mathrm{C} \end{bmatrix}, \quad \widetilde{\mathrm{D}} = \begin{bmatrix} \Delta\mathrm{D} \end{bmatrix}, \quad \widetilde{\boldsymbol{\Phi}} = \begin{bmatrix} \Phi \\ \phi \end{bmatrix},
$$

$$
\widetilde{\mathrm{E}}_{\mathrm{w}} = \begin{bmatrix} \bar{\mathrm{E}}_{\mathrm{w}} - \mathrm{L}\bar{\mathrm{F}}_{\mathrm{w}} \\ \bar{\mathrm{E}}_{\mathrm{w}} \end{bmatrix}, \quad \widetilde{\mathrm{E}}_{\mathrm{f}} = \begin{bmatrix} \mathrm{E_f} - \mathrm{LF_f} \\ \mathrm{E_f} \end{bmatrix}
$$

$$
\widetilde{\mathrm{F}}_{\mathrm{w}} = \begin{bmatrix} \bar{\mathrm{F}}_{\mathrm{w}} \end{bmatrix}, \quad \widetilde{\mathrm{F}}_{\mathrm{f}} = \begin{bmatrix} \mathrm{F_f} \end{bmatrix}.
$$

Thus, the error dynamics and residual vectors are given as

$$\begin{cases} \dot{\tilde{\mathbf{e}}} &= \widetilde{\mathrm{A}}\tilde{\mathbf{e}} + \widetilde{\mathrm{B}}\tilde{\mathbf{u}} + \widetilde{\mathrm{E}}_{\mathrm{w}}\tilde{\mathbf{w}} + \widetilde{\mathrm{E}}_{\mathrm{f}}\tilde{\mathbf{f}} + \widetilde{\mathbf{\Phi}} \\ \mathbf{r} &= \widetilde{\mathrm{C}}\tilde{\mathbf{e}} + \widetilde{\mathrm{D}}\tilde{\mathbf{u}} + \widetilde{\mathrm{F}}_{\mathrm{w}}\tilde{\mathbf{w}} + \widetilde{\mathrm{F}}_{\mathrm{f}}\tilde{\mathbf{f}} \end{cases}, \tag{10}$$

which will be used for fault detection [29].

C. ADAPTIVE THRESHOLD DESIGN

The following theorem establishes an adaptive threshold for fault detection in nonlinear systems.

Theorem 1. Given a scalar $\alpha \in \mathbb{R}_+$, if there exist $\gamma \in \mathbb{R}$ and a positive definite matrix P, such that the following inequalities hold

$$\begin{bmatrix} \mathrm{P} & 0 & 0 & \widetilde{\mathrm{C}}^\top \\ 0 & \mathrm{I} & 0 & \widetilde{\mathrm{F}}_{\mathrm{w}}^\top \\ 0 & 0 & \mathrm{I} & \widetilde{\mathrm{D}}^\top \\ \widetilde{\mathrm{C}} & \widetilde{\mathrm{F}}_{\mathrm{w}} & \widetilde{\mathrm{D}} & \gamma \mathrm{I} \end{bmatrix} \succ \mathbf{0} \tag{11}$$

$$\begin{bmatrix} \widetilde{\mathrm{A}}^\top \mathrm{P} + \mathrm{P}\widetilde{\mathrm{A}} + \alpha \mathrm{P} & \mathrm{P}\widetilde{\mathrm{E}}_{\mathrm{w}} & \mathrm{P}\widetilde{\mathrm{B}} & \mathrm{P} \\ \widetilde{\mathrm{E}}_{\mathrm{w}}^\top \mathrm{P} & 0 & 0 & 0 \\ \widetilde{\mathrm{B}}^\top \mathrm{P} & 0 & -\mathrm{I} & 0 \\ \mathrm{P} & 0 & 0 & 0 \end{bmatrix} \prec \mathbf{0} \tag{12}$$

Then, an adaptive threshold for the residual vector $\mathbf{r}$ is

$$\mathrm{J}_{\mathrm{th,adp}}(\mathrm{t}) = \sqrt{\gamma \times \left(\mathrm{e}^{-\alpha \mathrm{t}} * \tilde{\mathbf{u}}^\top \tilde{\mathbf{u}} + \bar{\mathrm{d}} + \tilde{\mathbf{u}}^\top \tilde{\mathbf{u}} \right)}. \tag{13}$$

Proof. Define $\mathrm{V} = \tilde{\mathbf{e}}^\top \mathrm{P}\, \tilde{\mathbf{e}}$, $\mathrm{W} = \tilde{\mathbf{w}}^\top \tilde{\mathbf{w}}$, and $\mathrm{U} = \tilde{\mathbf{u}}^\top \tilde{\mathbf{u}}$. We propose an upper bound for the residual norm square $\mathbf{r}^\top \mathbf{r}$ with $\gamma > 0$

$$\begin{aligned} \mathbf{r}^\top \mathbf{r} &\leq \gamma \times (\mathrm{V} + \mathrm{W} + \mathrm{U}) \\ &= \gamma \times \begin{bmatrix} \tilde{\mathbf{e}} \\ \tilde{\mathbf{w}} \\ \tilde{\mathbf{u}} \end{bmatrix}^\top \begin{bmatrix} \mathrm{P} & 0 & 0 \\ 0 & \mathrm{I} & 0 \\ 0 & 0 & \mathrm{I} \end{bmatrix} \begin{bmatrix} \tilde{\mathbf{e}} \\ \tilde{\mathbf{w}} \\ \tilde{\mathbf{u}} \end{bmatrix}. \end{aligned} \tag{14}$$

According to (10), $\mathbf{r}^\top \mathbf{r}$ can be rewritten as

$$\mathbf{r}^\top \mathbf{r} = \begin{bmatrix} \tilde{\mathbf{e}} \\ \tilde{\mathbf{w}} \\ \tilde{\mathbf{u}} \end{bmatrix}^\top \begin{bmatrix} \widetilde{\mathrm{C}}^\top \\ \widetilde{\mathrm{F}}_{\mathrm{w}}^\top \\ \widetilde{\mathrm{D}}^\top \end{bmatrix} \begin{bmatrix} \widetilde{\mathrm{C}} & \widetilde{\mathrm{F}}_{\mathrm{w}} & \widetilde{\mathrm{D}} \end{bmatrix} \begin{bmatrix} \tilde{\mathbf{e}} \\ \tilde{\mathbf{w}} \\ \tilde{\mathbf{u}} \end{bmatrix}. \tag{15}$$

Combining (15) and (14), we get

$$\begin{bmatrix} \tilde{\mathbf{e}} \\ \tilde{\mathbf{w}} \\ \tilde{\mathbf{u}} \end{bmatrix}^\top \left(\begin{bmatrix} \mathrm{P} & 0 & 0 \\ 0 & \mathrm{I} & 0 \\ 0 & 0 & \mathrm{I} \end{bmatrix} - \frac{1}{\gamma} \begin{bmatrix} \widetilde{\mathrm{C}}^\top \\ \widetilde{\mathrm{F}}_{\mathrm{w}}^\top \\ \widetilde{\mathrm{D}}^\top \end{bmatrix} \begin{bmatrix} \widetilde{\mathrm{C}} & \widetilde{\mathrm{F}}_{\mathrm{w}} & \widetilde{\mathrm{D}} \end{bmatrix} \right) \begin{bmatrix} \tilde{\mathbf{e}} \\ \tilde{\mathbf{w}} \\ \tilde{\mathbf{u}} \end{bmatrix} \geq 0, \tag{16}$$

which is equivalent to (11) by the Schur complement [30].

Consider the first-order derivative of V

$$\begin{aligned} \dot{\mathrm{V}} &= \dot{\tilde{\mathbf{e}}}^\top \mathrm{P}\tilde{\mathbf{e}} + \tilde{\mathbf{e}}^\top \mathrm{P}\dot{\tilde{\mathbf{e}}} \\ &= \left(\tilde{\mathbf{e}}^\top \widetilde{\mathrm{A}}^\top + \tilde{\mathbf{u}}^\top \widetilde{\mathrm{B}}^\top + \tilde{\mathbf{w}}^\top \widetilde{\mathrm{E}}_{\mathrm{w}}^\top + \widetilde{\mathbf{\Phi}}^\top \right) \mathrm{P}\tilde{\mathbf{e}} \\ &\quad + \tilde{\mathbf{e}}^\top \mathrm{P} \left(\widetilde{\mathrm{A}}\tilde{\mathbf{e}} + \widetilde{\mathrm{B}}\tilde{\mathbf{u}} + \widetilde{\mathrm{E}}_{\mathrm{w}}\tilde{\mathbf{w}} + \widetilde{\mathbf{\Phi}} \right) \\ &= \begin{bmatrix} \tilde{\mathbf{e}} \\ \tilde{\mathbf{w}} \\ \tilde{\mathbf{u}} \\ \widetilde{\mathbf{\Phi}} \end{bmatrix}^\top \begin{bmatrix} \widetilde{\mathrm{A}}^\top \mathrm{P} + \mathrm{P}\widetilde{\mathrm{A}} & \mathrm{P}\widetilde{\mathrm{E}}_{\mathrm{w}} & \mathrm{P}\widetilde{\mathrm{B}} & \mathrm{P} \\ \widetilde{\mathrm{E}}_{\mathrm{w}}^\top \mathrm{P} & 0 & 0 & 0 \\ \widetilde{\mathrm{B}}^\top \mathrm{P} & 0 & 0 & 0 \\ \mathrm{P} & 0 & 0 & 0 \end{bmatrix} \begin{bmatrix} \tilde{\mathbf{e}} \\ \tilde{\mathbf{w}} \\ \tilde{\mathbf{u}} \\ \widetilde{\mathbf{\Phi}} \end{bmatrix}. \end{aligned} \tag{17}$$

Given an appropriate value for α, $\dot{\mathrm{V}}$ can be upper-bounded as

$$\dot{\mathrm{V}} \leq -\alpha \mathrm{V} + \tilde{\mathbf{u}}^\top \tilde{\mathbf{u}}, \tag{18}$$

which can be rewritten as:

$$\begin{bmatrix} \tilde{\mathbf{e}} \\ \tilde{\mathbf{w}} \\ \tilde{\mathbf{u}} \\ \widetilde{\mathbf{\Phi}} \end{bmatrix}^\top \begin{bmatrix} \widetilde{\mathrm{A}}^\top \mathrm{P} + \mathrm{P}\widetilde{\mathrm{A}} + \alpha \mathrm{P} & \mathrm{P}\widetilde{\mathrm{E}}_{\mathrm{w}} & \mathrm{P}\widetilde{\mathrm{B}} & \mathrm{P} \\ \widetilde{\mathrm{E}}_{\mathrm{w}}^\top \mathrm{P} & 0 & 0 & 0 \\ \widetilde{\mathrm{B}}^\top \mathrm{P} & 0 & -\mathrm{I} & 0 \\ \mathrm{P} & 0 & 0 & 0 \end{bmatrix} \begin{bmatrix} \tilde{\mathbf{e}} \\ \tilde{\mathbf{w}} \\ \tilde{\mathbf{u}} \\ \widetilde{\mathbf{\Phi}} \end{bmatrix} \leq 0 \tag{19}$$

yielding (12). Furthermore, from (18) we get

$$\begin{aligned} \mathrm{V} &\leq \mathrm{e}^{-\alpha \mathrm{t}} \mathrm{V}(0) + \int_0^{\mathrm{t}} \mathrm{e}^{-\alpha(\mathrm{t}-\tau)} \left[\tilde{\mathbf{u}}^\top \tilde{\mathbf{u}} \right] \mathrm{d}\tau \\ &= \int_0^{\mathrm{t}} \mathrm{e}^{-\alpha(\mathrm{t}-\tau)} \left[\tilde{\mathbf{u}}^\top \tilde{\mathbf{u}} \right] \mathrm{d}\tau \\ &= \mathrm{e}^{-\alpha \mathrm{t}} * \tilde{\mathbf{u}}^\top \tilde{\mathbf{u}}. \end{aligned} \tag{20}$$

By setting $\tilde{\mathbf{w}}^\top \tilde{\mathbf{w}} \leq \bar{\mathrm{d}}$, we have

$$\mathbf{r}^\top \mathbf{r} \leq \gamma \times \left(\mathrm{e}^{-\alpha \mathrm{t}} * \tilde{\mathbf{u}}^\top \tilde{\mathbf{u}} + \bar{\mathrm{d}} + \tilde{\mathbf{u}}^\top \tilde{\mathbf{u}} \right).$$

Therefore, we obtain the adaptive threshold as

$$\mathrm{J}_{\mathrm{th,dyn}} = \sqrt{\gamma \times \left(\mathrm{e}^{-\alpha \mathrm{t}} * \tilde{\mathbf{u}}^\top \tilde{\mathbf{u}} + \bar{\mathrm{d}} + \tilde{\mathbf{u}}^\top \tilde{\mathbf{u}} \right)}.$$

□

We can minimize the upper bound by solving the following semidefinite program

$$\boxed{\begin{array}{ll} \underset{\gamma \in \mathbb{R}, \mathrm{P} \succ 0}{\text{minimize}} & \gamma \\ \text{subject to} & (11) - (12). \end{array}}$$

Due to the polytopic uncertainty of the nonlinear system, the LMIs (11) and (12) represent infinite LMI constraints, making the optimization problem infinite-dimensional and not tractable. To deal with this problem, let us introduce the following theorem

Theorem 2 (see [31]). The following are equivalent for any H, L_i, R_i.

$$\mathrm{H} + \sum_\mathrm{i} \mathrm{L}_\mathrm{i} \Delta \mathrm{R}_\mathrm{i} \succ \mathbf{0} \quad \forall\, \Delta \in \mathrm{Co}\left(\Delta_1, \ldots, \Delta_\mathrm{k}\right) \tag{21}$$

$$\mathrm{H} + \sum_\mathrm{i} \mathrm{L}_\mathrm{i} \Delta_\mathrm{j} \mathrm{R}_\mathrm{i} \succ \mathbf{0} \quad \forall\, \mathrm{j} = 1, \ldots, \mathrm{k} \tag{22}$$

The theorem says that the LMIs with polytopic uncertainty only need to hold at the vertices of the polytope [31]. To apply Theorem 2 to the LMIs in (11) and (12), we set $L_i = R_i = 1$ with $i = 1$ in (22), and follow a series of mathematical operations that transform the LMIs into a finite set expressed as

$$\begin{bmatrix} P & 0 & 0 & \widetilde{C}_o^\top \\ 0 & I & 0 & \widetilde{F}_{wo}^\top \\ 0 & 0 & I & \widetilde{D}_o^\top \\ \widetilde{C}_o & \widetilde{F}_{wo} & \widetilde{D}_o & \gamma I \end{bmatrix} + \begin{bmatrix} 0 & 0 & 0 & \Delta\widetilde{C}_i^\top \\ 0 & 0 & 0 & \Delta\widetilde{F}_{wi}^\top \\ 0 & 0 & 0 & \Delta\widetilde{D}_i^\top \\ \Delta\widetilde{C}_i & \Delta\widetilde{F}_{wi} & \Delta\widetilde{D}_i & 0 \end{bmatrix} \succ \mathbf{0} \quad \forall i = 1, \ldots, p$$

$$\begin{bmatrix} \widetilde{A}_o^\top P + P\widetilde{A}_o + \alpha P & P\widetilde{E}_{wo} & P\widetilde{B}_o & P \\ \widetilde{E}_{wo}^\top P & 0 & 0 & 0 \\ \widetilde{B}_o^\top P & 0 & -I & 0 \\ P & 0 & 0 & 0 \end{bmatrix} + \begin{bmatrix} \Delta\widetilde{A}_i^\top P + P\Delta\widetilde{A}_i & P\Delta\widetilde{E}_{wi} & P\Delta\widetilde{B}_i & 0 \\ \Delta\widetilde{E}_{wi}^\top P & 0 & 0 & 0 \\ \Delta\widetilde{B}_i^\top P & 0 & 0 & 0 \\ 0 & 0 & 0 & 0 \end{bmatrix} \prec \mathbf{0} \quad \forall i = 1, \ldots, p$$

where

$$\widetilde{A}_o = \begin{bmatrix} A - LC & 0 \\ 0 & A \end{bmatrix}, \quad \widetilde{B}_o = \begin{bmatrix} 0 \\ B \end{bmatrix},$$

$$\widetilde{C}_o = \begin{bmatrix} C & 0 \end{bmatrix}, \quad \widetilde{D}_o = [0],$$

$$\widetilde{E}_{wo} = \begin{bmatrix} E_w - LF_w \\ E_w \end{bmatrix}, \quad \widetilde{F}_{wo} = [F_w],$$

$$\Delta\widetilde{A}_i = \begin{bmatrix} 0 & \Delta A_i - L\Delta C_i \\ 0 & \Delta A_i \end{bmatrix}, \quad \Delta\widetilde{B}_i = \begin{bmatrix} \Delta B_i - L\Delta D_i \\ \Delta B_i \end{bmatrix},$$

$$\Delta\widetilde{C}_i = \begin{bmatrix} 0 & \Delta C_i \end{bmatrix}, \quad \Delta\widetilde{D}_i = [\Delta D_i],$$

$$\Delta\widetilde{E}_i = \begin{bmatrix} \Delta E_{wi} - L\Delta F_{wi} \\ \Delta E_{wi} \end{bmatrix}, \quad \Delta\widetilde{F}_{wi} = [\Delta F_{wi}].$$

D. EVALUATION OF THE RESIDUAL

We follow the protocol presented in [32] to decide whether a fault occurs. We define the function that evaluates the residual as $J = \|\mathbf{r}\|_2$. Ideally, during a fault-free scenario, the value of J must be zero and strictly positive. Nonetheless, J is strictly positive even when a fault is absent due to the presence of disturbances. The adaptive threshold is set by considering the system is in the absence of faults and subjected to disturbances. The rule for detecting a fault is defined as

$$\begin{cases} \text{Absence of faults,} & \text{if } J \leq J_{th} \\ \text{Fault alarm,} & \text{if } J > J_{th}. \end{cases} \tag{23}$$

An essential component in any scheme for detecting faults is the threshold J_{th}. A trustworthy threshold reduces the chances of false alarms and missed detection while enhancing the fault detection capability.

TABLE 1: Parameters of the Grid-Forming Inverters.

Parameter	Value	
	#1 GFM	#3 GFM
Power rating (kVA)	45	34
Voltage rating (V)	380	380
m_{Pi}	9.4×10^{-5}	12.5×10^{-5}
n_{Qi}	1.3×10^{-3}	1.5×10^{-3}
R_{ci} (Ω)	0.03	0.03
L_{ci} (mH)	0.35	0.35
R_{fi} (Ω)	0.1	0.1
L_{fi} (mH)	1.35	1.35
C_{fi} (μF)	50	50
K_{PVi}	0.1	0.05
K_{IVi}	420	390
K_{PCi}	15	10.5
K_{ICi}	20000	16000
ω_b (rad/s)	314.16	314.16

TABLE 2: Parameters of the AC microgrid.

	Parameter	Value
Branch 1	R_{br}	0.23 Ω
	L_{br}	318 μH
Branch 2	R_{br}	0.35 Ω
	L_{br}	1847 μH
Branch 3	R_{br}	0.23 Ω
	L_{br}	318 μH
Load 1	R_{lo}	30 Ω
	L_{lo}	477 mH
Load 2	R_{lo}	20 Ω
	L_{lo}	318 mH
Load 3	R_{lo}	25 Ω
	L_{lo}	318 mH
Load 4	R_{lo}	25 Ω
	L_{lo}	477 mH

IV. NUMERICAL TESTS

The simulations were run using Matlab and Simulink. We use the YALMIP toolbox and the SDPT3 solver to solve the optimization problem in Theorem 1. All simulations correspond to the grid-forming inverter selected as the reference generator. Similar simulation results were obtained for the remaining inverters in the microgrid test system. Our proposed adaptive threshold is compared with a fixed threshold approach described in a recent work [29]. The disturbance matrices are designed as $E_w = B$ and $F_w = D$. The busbar fault is modeled as $E_f = [B_4\, B_5]$, and $F_f = \mathbf{0}$, whereas the sensor fault is modeled as $E_f = \mathbf{0}$, and $F_f = 1$. The parameter values for the residual thresholds are

TABLE 3: Parameters of the adaptive threshold for the busbar and sensor faults.

	Busbar Fault	Sensor Fault
γ	0.493	0.026
α	1.290	0.121

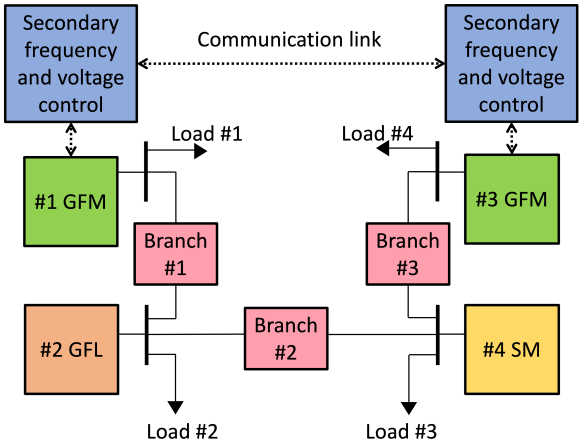

FIGURE 2: Single line diagram of the AC microgrid test system.

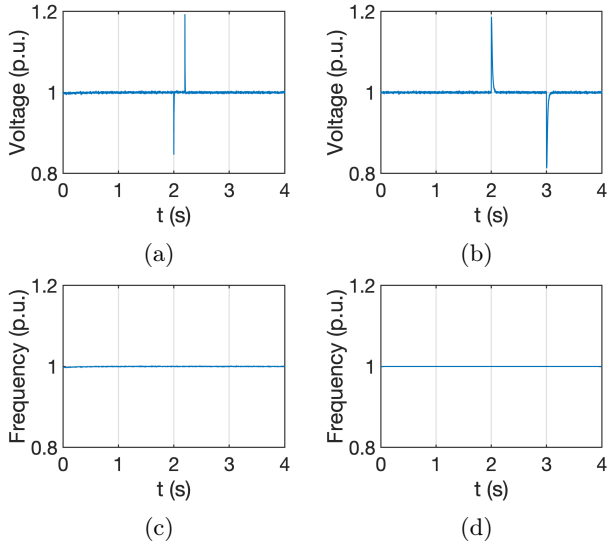

FIGURE 3: Impact of the internal faults on the voltage magnitude (p.u.) and frequency (p.u.). (a) and (c) busbar fault during 0.2 seconds; (b) and (d) sensor fault during 1 second.

presented in Table 3. We select the parameters of the LC filter as the uncertain parameters. Consequently, the vertices of the polytope $\{\Xi_1, \ldots, \Xi_p\}$ are obtained by uniformly selecting values of these parameters within two percent of the nominal rating shown in Table 1. The number of vertices of the polytope is set to $p = 5$.

A. MICROGRID TEST SYSTEM

We implement the islanded AC microgrid, shown in Fig. 2, to test the proposed adaptive threshold. The microgrid consists of two GFMs, one GFL, one SG, four busbars, four loads, and three inductive RL branches. The parameters and data of the GFMs and microgrid are shown in Tables 1 and 2. GFM #1 is selected as the reference generator. The GFMs are locally controlled by the virtual synchronous machine technique (GFM #1) and droop curves (GFM #2) [23]. In addition, the voltage magnitude and frequency reference of the GFMs are regulated by a secondary control layer as described in [22]. The parameters of the GFL can be found in [22]. We consider the classical fourth-order nonlinear model for the SG [33] with a BPA-GG governor [34] and low-order exciter [35].

B. BUSBAR FAULT

The bus at the point of common coupling, which is the bus that connects the GFM with the microgrid, may be subject to a busbar fault. The busbar fault is implemented as a symmetrical fault corresponding to the sudden change of the PCC's voltage magnitude (v_{bi}). Fig. 3a and Fig. 3c present the impact of the busbar fault in the inverter's output voltage magnitude (v_{oi}) and frequency (ω_i). The figures show that the busbar fault perturbs the voltage magnitude at the PCC by decreasing it when the fault occurs and increasing it when the fault is cleared. We observe that the inverter's frequency remains idle during the presence of the fault. In other words, the effects of the busbar fault are decoupled between the voltage magnitude and frequency.

The following analysis explains the reason for this phenomenon. The voltage magnitude droop $\omega_i = \omega_{ni} - m_{Pi}P_i$ is equivalent to $\omega_i = \omega_{ni} - \Delta\omega$ and a characteristic swing equation $\dot{\Delta\omega} = \frac{1}{J_i}(P_{i,uf} - D_i\Delta\omega)$, where J_i, D_i, $P_{i,uf}$ are the equivalent synthetic inertia, damping, and the unfiltered active power measurement for the i-th GFM, respectively. Notice that the product $\frac{1}{J_i}P_{i,uf}$ is exceedingly diminutive because the equivalent inertia J_i is inversely proportional to the droop coefficient m_{Pi}, which is in the order of 10^{-5}. Hence, any change in the unfiltered active power $P_{i,uf}$ due to the busbar fault does not largely influence the dynamics of $\Delta\omega$.

Fig. 4a shows the adaptive threshold and residual norm response when a busbar fault occurs at time $t = 2$ s at the PCC. After 0.2 seconds, the busbar fault is cleared at time $t = 2.2$ s. Both thresholds remain above the residual during the absence of the fault in the entire simulation horizon. We observe that the adaptive threshold decreases rapidly below the residual norm when the fault happens, as shown in the left magnified box. The fault is detected as early as 0.01 milliseconds. Notice that the adaptive threshold quickly responds to the fault presence, which makes the fault detection fast. On the other hand, using a fixed threshold takes almost

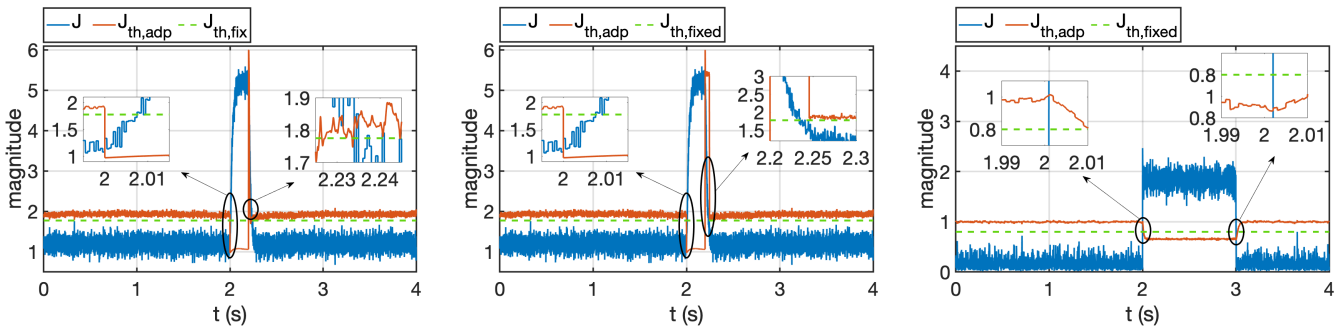

(a) (b) (c)

FIGURE 4: Residual norm, adaptive and fixed threshold comparison. (a) Busbar fault. (b) Busbar fault with postprocessing. (c) Sensor fault in v^*_{odi}.

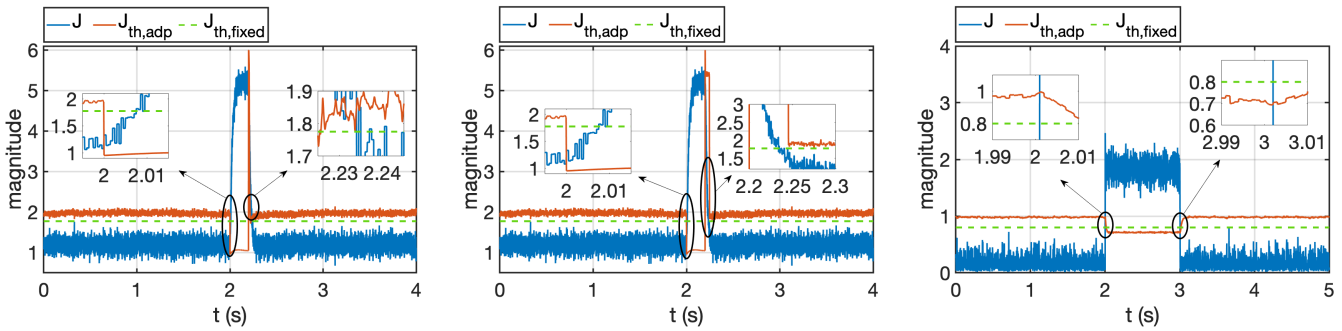

(a) (b) (c)

FIGURE 5: Residual norm, adaptive and fixed threshold comparison with modeling errors. (a) Busbar fault. (b) Busbar fault with postprocessing. (c) Sensor fault in v^*_{odi}.

ten milliseconds to detect the busbar fault. In the right magnified box, we observe the behavior of the thresholds when the fault is cleared. Both thresholds yield similar clearing times because it takes about 40 milliseconds to restore the fault-free condition.

Postprocessing of the adaptive threshold can be used to reduce the threshold's fault-clearing time. In Fig. 4a, we observe that the adaptive threshold reaches a maximum value of about six when the busbar fault is cleared at time t = 2.2 s. This is because the threshold is computed using the input vector $\mathbf{u}$, which is severely affected by the bus voltages v_{bdi} and v_{bqi} when the busbar fault occurs. Fig. 4b presents the post-processed response of the adaptive threshold and the residual norm. The postprocessing consists of holding the value of the dynamic residual for approximately 30 milliseconds as soon as the maximum value of the threshold is detected, i.e., immediately after the fault is cleared. The threshold follows its original value afterward. A limitation of such an approach is that a busbar fault cannot be detected while postprocessing takes effect.

C. SENSOR FAULT

The sensor fault is implemented as a sudden increase in v^*_{odi}, the reference voltage for the GFM's voltage controller, corresponding to at least the 10% of its steady-state value. A sudden change above 10% will excite the residual norm sufficiently for our proposed adaptive threshold to detect the fault. Fig. 3b and Fig. 3d present the impact of the sensor fault in the inverter's output voltage magnitude (v_{oi}) and frequency (ω_i). We notice that the fault is observable in the voltage magnitude rather than in the frequency. The explanation for this phenomenon is the same as the explanation given for the busbar fault in Section IV-B. Fig. 3b shows that the inverter's voltage controller immediately reacts at t = 2 s in opposition to the detected increase in v^*_{odi} by reducing the output voltage magnitude v_{odi} and maintaining it around its pre-fault value. A similar situation occurs when the fault is cleared at t = 3 s.

Fig. 4c presents the responses of the residual norm, dynamic, and fixed thresholds under a v^*_{odi} sensor fault. The sensor fault occurs at time t = 2 s and is cleared at t = 3 s. We observe that the adaptive threshold obeys the desired detection logic during the entire horizon. The adaptive threshold remains above the residual norm during fault-free intervals and below the norm during fault occurrence. The proposed adaptive threshold minimizes the rates of false alarms and missed detection to zero. Notice that the adaptive threshold allows for

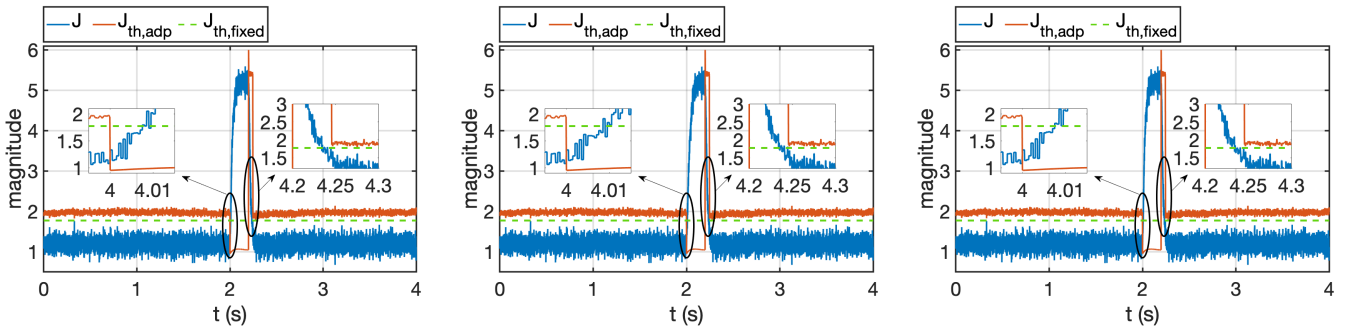

(a) (b) (c)

FIGURE 6: Response of the residual norm, fixed threshold, and adaptive threshold with postprocessing and modeling errors under a busbar fault using nonlinear loads with (a) $\mathbf{v} = [\mathrm{v}_{\mathrm{bdi}}^2 \;\; \mathrm{v}_{\mathrm{bqi}}^2]^\top$, (b) $\mathbf{v} = [\mathrm{v}_{\mathrm{bdi}}^4 \;\; \mathrm{v}_{\mathrm{bqi}}^4]^\top$, (c) $\mathbf{v} = [\mathrm{v}_{\mathrm{bdi}}\mathrm{i}_{\mathrm{lod_i}} \;\; \mathrm{v}_{\mathrm{bqi}}\mathrm{i}_{\mathrm{lod_i}}]^\top$.

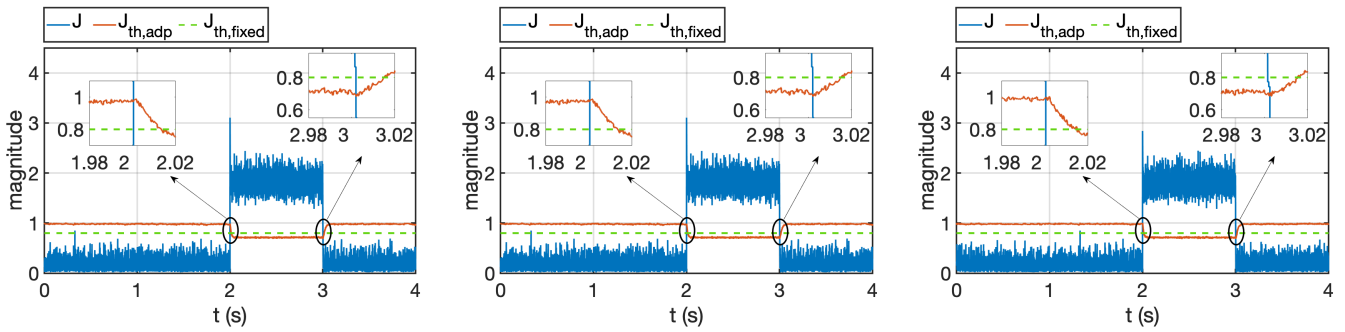

(a) (b) (c)

FIGURE 7: Response of the residual norm, fixed threshold, and adaptive threshold with modeling errors under a sensor fault using nonlinear loads with (a) $\mathbf{v} = [\mathrm{v}_{\mathrm{bdi}}^2 \;\; \mathrm{v}_{\mathrm{bqi}}^2]^\top$, (b) $\mathbf{v} = [\mathrm{v}_{\mathrm{bdi}}^4 \;\; \mathrm{v}_{\mathrm{bqi}}^4]^\top$, (c) $\mathbf{v} = [\mathrm{v}_{\mathrm{bdi}}\mathrm{i}_{\mathrm{lod_i}} \;\; \mathrm{v}_{\mathrm{bqi}}\mathrm{i}_{\mathrm{loq_i}}]^\top$.

a fast detection of around 0.01 milliseconds. Also, it can be seen that the fixed threshold is tighter than the adaptive threshold. However, the adaptive threshold stays farther from the residual than the fixed threshold. Such a distance may help to avoid false alarms and missed detections under potential new disturbances.

D. MODELING ERRORS

To account for the influence of modeling errors, we double the resistance ($\mathrm{R_{fi}}$), inductance ($\mathrm{L_{fi}}$), and capacitance ($\mathrm{C_{fi}}$) values of the LC filter. Also, we double the resistance ($\mathrm{R_{ci}}$) and inductance ($\mathrm{L_{ci}}$) values of the output connector. Meanwhile, the adaptive threshold parameters are the same as those presented in Table 3. Fig. 5a, 5b, and 5c show the response of the adaptive threshold with modeling errors for the busbar fault and sensor fault, respectively. The figures show that the thresholds still follow the same response as the original ones without errors. The adaptive threshold for busbar fault exhibits a slight positive bias; see Fig. 5a and 5b. The adaptive threshold for the sensor fault presents a small negative bias; see Fig. 5c.

E. NONLINEAR LOADS

We evaluate the merits of our proposed adaptive threshold design using three types of nonlinear loads by running experiments for both busbar and sensor faults. In general, the dynamics of the loads in the dq domain are expressed as $\dot{\mathbf{i}}_{\mathrm{lo}} = \mathrm{J}\,\mathbf{i}_{\mathrm{lo}} + \mathbf{v}$ where $\mathbf{i}_{\mathrm{lo}} = [\mathrm{i}_{\mathrm{lodi}} \;\; \mathrm{i}_{\mathrm{loqi}}]^\top$, $\mathbf{v} = [\mathrm{v}_{\mathrm{bdi}} \;\; \mathrm{v}_{\mathrm{bqi}}]^\top$ and

$$\mathrm{J} = \begin{bmatrix} -\frac{\mathrm{R_{lo}}}{\mathrm{L_{lo}}} & \omega_{\mathrm{r}} \\ -\omega_{\mathrm{r}} & -\frac{\mathrm{R_{lo}}}{\mathrm{L_{lo}}} \end{bmatrix}.$$

We modify $\mathbf{v}$ as a two-dimensional vector with entries nonlinear in terms of $\mathrm{v_{bdi}}$ and $\mathrm{v_{bqi}}$ to model the nonlinear models. For these experiments, we consider three types of nonlinear loads defined by $\mathbf{v} = [\mathrm{v}_{\mathrm{bdi}}^2 \;\; \mathrm{v}_{\mathrm{bqi}}^2]^\top$, $\mathbf{v} = [\mathrm{v}_{\mathrm{bdi}}^4 \;\; \mathrm{v}_{\mathrm{bqi}}^4]^\top$, and $\mathbf{v} = [\mathrm{v_{bdi}i_{lodi}} \;\; \mathrm{v_{bqi}i_{loqi}}]^\top$. Figures 6, and 7 show that the response of our adaptive threshold design remains almost invariant to the three types of nonlinear load dynamics across all the experiments. Such a result is congruent with the fault modeling and state-space representation of the inverter that considers the rest of the microgrid and its components as external entities. Notice that, from the GFM side, the dynamics of the nonlinear loads and other microgrid components

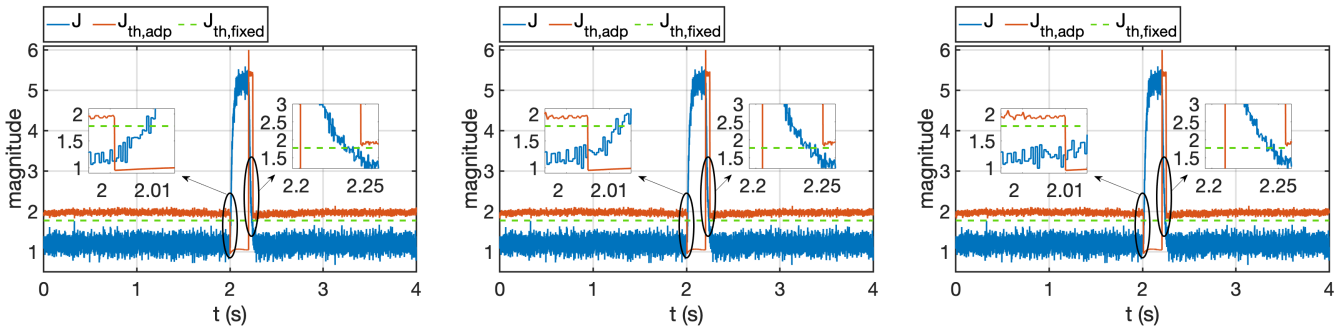

(a) (b) (c)

FIGURE 8: Response of the residual norm, fixed threshold, and adaptive threshold with postprocessing and modeling errors under a busbar fault with an input delay of (a) d = 1 ms, (b) d = 5 ms, (c) d = 10 ms.

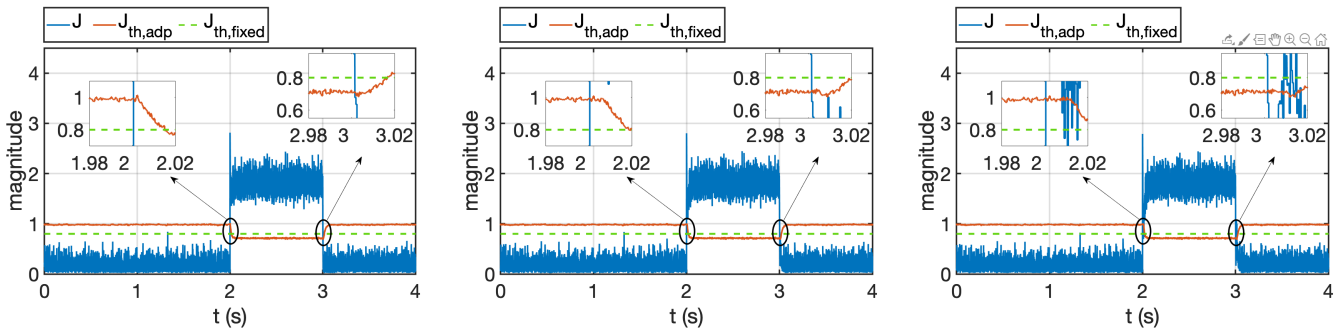

(a) (b) (c)

FIGURE 9: Response of the residual norm, fixed threshold, and adaptive threshold with modeling errors under a sensor fault with an input delay of (a) d = 1 ms, (b) d = 5 ms, (c) d = 10 ms.

show up in the bus voltage magnitudes v_{bdi} and v_{bqi}, which are inputs of the state-space GFM modeling. Despite these results, we acknowledge that other types of nonlinear loads should be used to test the robustness of our approach. Nonetheless, these preliminary results show that our adaptive threshold design achieves an accurate response in the presence of the considered nonlinear loads.

F. INPUT DELAYS

In this section, we evaluate the performance of the proposed approach when the input vector $\mathbf{u}$ is delayed d units of time. Notice that three out of five input signals, ω_r, ω_{ni}, and V_{ni} might be subject to delays because these signals travel through the communication network established by the secondary control layer. The other two input signals, the dq bus voltage magnitudes (v_{bdi}) and (v_{bqi}), are not influenced by the communication delays because they are physical signals. Figures 8 and 9 show the response of the residual norm, fixed threshold, and adaptive threshold with postprocessing and modeling errors under a busbar and sensor fault for input delays of 1 ms, 5 ms, and 10 ms. We observe that the input delay setbacks the response of the adaptive threshold proportionally to the value of d. The higher the delay d, the longer the adaptive threshold responds to the fault occurrence or clearance. Figures 8a and 9a show that the response of the adaptive threshold and residual norm preserve the accuracy of the fault detection logic. However, as shown in Figure 9c, when the delay is d = 10 ms, both the observer residual and adaptive threshold do not synchronize correctly, leading to unwanted outcomes of the detection logic for almost 5 ms.

TABLE 4: Comparison of the proposed method with other fault detection techniques.

Methods	Focus on GFMs	Response Time	Type of Threshold	Type of Faults
[36]	No	Medium	Adaptive	Sensor
[37]	Yes	Slow	Fixed	Busbar
Proposed	Yes	Fast	Adaptive	Busbar& Sensor

V. DISCUSSION

A. APPLICABILITY OF THE PROPOSED METHOD

The observer and adaptive threshold can be merged into one module that exchanges inputs and outputs with the inverter's sensor and controller. The module can be implemented in real-time within the inverter's embedded microcontroller as code written in any programming

language with appropriate software libraries. The processing extra burden exerted over the microcontroller is minimal due to the advancements in computational processing power for microcontrollers. A significant advantage of our approach is that its implementation requires no additional hardware because the module uses signals already measured by the grid-forming inverter. Such a solution is cost-effective, with the additional benefit of making it an entirely internal solution where other external information is not required.

B. COMPARISON WITH SIMILAR DETECTION TECHNIQUES

Table 4 compares our proposed method with similar fault detection techniques for inverters operating in islanded AC microgrids. The comparison aims to assess the efficacy and limitations of the techniques presented in [36] and [37]. The authors in [36] develop a model- and observer-based fault detection strategy with an adaptive threshold to protect inverters. Although the strategy exhibits a medium detection speed, the method is tested on grid-side converters and is limited to sensor faults. Also, the adaptive threshold shows low sensitivity to faults, causing missed and false detections. In [37], the authors develop a signal-based strategy that superimposes current components and combines them with a voltage restraint quantity. Even though the method can capture the presence of faults, it introduces a windowing strategy to compute the restraint threshold, delaying the detection of the fault. Our proposed method overcomes the drawbacks of these works by effectively designing an adaptive threshold that minimizes misdetections and timely detects faults.

C. LIMITATIONS

The grid-forming inverters operate under the regulation of a secondary control layer that relies on a communication network. Our proposed approach will be affected by network delays because it uses the state-space input signals transported through the network's communication channels. Although the convergence of the observer with input delays is guaranteed, its response will be delayed, delaying the residual signal used to compare it with the adaptive threshold. It is beyond the scope of this work to design an observer robust to input delays because our goal is to design an adaptive threshold for residual-based fault detection. We assume that such an observer has already been designed and provided. The designed adaptive threshold performs well with input delays of less than 10 ms but will exhibit a slow response for longer delays. For this reason, we suggest that our proposed adaptive threshold should be chosen for secondary control layers running over a low-latency communication protocol such as DNP3 Ethernet [38], [39].

D. FUTURE WORK

Despite the merits of our proposed fault detection adaptive threshold design for grid-forming inverters, our method requires further analysis for its immediate application to inverter-dominant large-scale power systems. The fundamental reason is that large-scale power systems with high penetration of inverters bring significant stability challenges [40]. The dynamics of inverters and their controls operate on a similar time scale as the line dynamics, which can result in resonance phenomena and, ultimately, instability. In addition, the imbalance in microgrids is a known power quality issue that leads to harmful effects such as increased neutral currents and voltages, power oscillations, and equipment malfunctioning [41]. In this regard, we suggest additional tests of our proposed method under asymmetric currents in islanded microgrids. Furthermore, efforts to underground power lines to reduce wildfire risk will require our proposed method to handle capacitive lines. We leave these investigations as part of future endeavors.

VI. CONCLUSION

This paper develops an adaptive threshold strategy for GFMs in islanded-mode AC microgrids. The proposed threshold is computed as an upper bound on the ℓ_2 norm of the residual vector under a fault-free condition. The bound parameters are successfully obtained by solving a semidefinite program with two constraints of linear matrix inequalities. A microgrid with two GFMs, one GFL, and one synchronous machine is used to evaluate the performance of the proposed threshold under a busbar and sensor fault. The GFMs are synchronized with a secondary control for the frequency and voltage magnitude. The numerical results show our proposed approach's practical contributions, effectiveness, and implementation feasibility. Moreover, the proposed adaptive threshold alleviates the issues of using a fixed threshold, which may introduce false alarms or missed detections.

APPENDIX.

A. GFM DYNAMIC EQUATIONS

The dynamic equations of the inverter's auxiliary variables are given as

$$\dot{\phi}_{\mathrm{di}} = \mathrm{v}^{*}_{\mathrm{odi}} - \mathrm{v}_{\mathrm{odi}}, \tag{24a}$$

$$\dot{\phi}_{\mathrm{qi}} = -\mathrm{v}_{\mathrm{oqi}}, \tag{24b}$$

$$\dot{\gamma}_{\mathrm{di}} = \mathrm{F_i i_{odi}} - \omega_{\mathrm{b}} \mathrm{C_{fi}} \mathrm{v_{oqi}} + \mathrm{K_{PVi}} \mathrm{v}^{*}_{\mathrm{odi}} - \mathrm{K_{PVi}} \mathrm{v_{odi}} + \mathrm{K_{IVi}} \phi_{\mathrm{di}} - \mathrm{i_{ldi}}, \tag{24c}$$

$$\dot{\gamma}_{\mathrm{qi}} = \mathrm{F_i i_{oqi}} + \omega_{\mathrm{b}} \mathrm{C_{fi}} \mathrm{v_o di} - \mathrm{K_{PVi}} \mathrm{v_{oqi}} + \mathrm{K_{IVi}} \phi_{\mathrm{qi}} - \mathrm{i_{lqi}}. \tag{24d}$$

The dynamic equations governing the inverter's power angle, active power, and reactive power are presented as

follows

$$\dot{\delta}_{\mathrm{i}} = \omega_{\mathrm{i}} - \omega_{\mathrm{r}}, \tag{25a}$$

$$\dot{\mathrm{P}}_{\mathrm{i}} = -\omega_{\mathrm{ci}}\mathrm{P}_{\mathrm{i}} + \omega_{\mathrm{ci}}(\mathrm{v}_{\mathrm{odi}}\mathrm{i}_{\mathrm{odi}} + \mathrm{v}_{\mathrm{oqi}}\mathrm{i}_{\mathrm{oqi}}), \tag{25b}$$

$$\dot{\mathrm{Q}}_{\mathrm{i}} = -\omega_{\mathrm{ci}}\mathrm{Q}_{\mathrm{i}} + \omega_{\mathrm{ci}}(\mathrm{v}_{\mathrm{oqi}}\mathrm{i}_{\mathrm{odi}} - \mathrm{v}_{\mathrm{odi}}\mathrm{i}_{\mathrm{oqi}}). \tag{25c}$$

The differential equations of the inverter's output current magnitudes, voltage magnitudes, and LC filter output current magnitudes are

$$\dot{\mathrm{i}}_{\mathrm{ldi}} = -\frac{\mathrm{R}_{\mathrm{fi}}}{\mathrm{L}_{\mathrm{fi}}}\mathrm{i}_{\mathrm{ldi}} + \omega_{\mathrm{ni}}\mathrm{i}_{\mathrm{lqi}} + \frac{1}{\mathrm{L}_{\mathrm{fi}}}(\mathrm{v}_{\mathrm{idi}} - \mathrm{v}_{\mathrm{odi}}), \tag{26a}$$

$$\dot{\mathrm{i}}_{\mathrm{lqi}} = -\frac{\mathrm{R}_{\mathrm{fi}}}{\mathrm{L}_{\mathrm{fi}}}\mathrm{i}_{\mathrm{lqi}} - \omega_{\mathrm{ni}}\mathrm{i}_{\mathrm{ldi}} + \frac{1}{\mathrm{L}_{\mathrm{fi}}}(\mathrm{v}_{\mathrm{iqi}} - \mathrm{v}_{\mathrm{oqi}}), \tag{26b}$$

$$\dot{\mathrm{v}}_{\mathrm{odi}} = \omega_{\mathrm{ni}}\mathrm{v}_{\mathrm{oqi}} + \frac{1}{\mathrm{C}_{\mathrm{fi}}}(\mathrm{i}_{\mathrm{ldi}} - \mathrm{i}_{\mathrm{odi}}), \tag{26c}$$

$$\dot{\mathrm{v}}_{\mathrm{oqi}} = -\omega_{\mathrm{ni}}\mathrm{v}_{\mathrm{odi}} + \frac{1}{\mathrm{C}_{\mathrm{fi}}}(\mathrm{i}_{\mathrm{lqi}} - \mathrm{i}_{\mathrm{oqi}}), \tag{26d}$$

$$\dot{\mathrm{i}}_{\mathrm{odi}} = -\frac{\mathrm{R}_{\mathrm{ci}}}{\mathrm{L}_{\mathrm{ci}}}\mathrm{i}_{\mathrm{odi}} + \omega_{\mathrm{ni}}\mathrm{i}_{\mathrm{oqi}} + \frac{1}{\mathrm{L}_{\mathrm{ci}}}(\mathrm{v}_{\mathrm{odi}} - \mathrm{v}_{\mathrm{bdi}}), \tag{26e}$$

$$\dot{\mathrm{i}}_{\mathrm{oqi}} = -\frac{\mathrm{R}_{\mathrm{ci}}}{\mathrm{L}_{\mathrm{ci}}}\mathrm{i}_{\mathrm{oqi}} - \omega_{\mathrm{ni}}\mathrm{i}_{\mathrm{odi}} + \frac{1}{\mathrm{L}_{\mathrm{ci}}}(\mathrm{v}_{\mathrm{oqi}} - \mathrm{v}_{\mathrm{bqi}}). \tag{26f}$$

B. GFM NONLINEAR TERM AS A ONE-SIDED LIPSCHITZ FUNCTION

The observer design necessitates the nonlinearity $\boldsymbol{\phi}(\mathbf{x}, \mathbf{u})$ to be one-sided Lipschitz continuous, defined as

Definition 1. The function $\mathrm{f}(\cdot)$ is one-sided Lipschitz continuous if a constant $\rho \in \mathbb{R}$ exists such that $\forall\, \mathbf{u} \in \mathcal{U}$ and $\forall\, \mathbf{x}, \hat{\mathbf{x}} \in \mathcal{D}$:

$$\langle \mathrm{f}(\mathbf{x}, \mathbf{u}) - \mathrm{f}(\hat{\mathbf{x}}, \mathbf{u}), \mathbf{x} - \hat{\mathbf{x}} \rangle \leq \rho \|\mathbf{x} - \hat{\mathbf{x}}\|^2. \tag{27}$$

The constant ρ is obtained by sampling the states-inputs operating region $(\mathcal{D} \times \mathcal{U})$ of the GFM such that each interval contains equally spaced sample points. We select 100 sample points per interval by acknowledging the trade-off between computational burden and a denser sample space for a more precise constant calculation. According to [25], the one-sided Lipschitz constant can be computed as $\rho = \limsup\left(\alpha\left(\frac{\partial \boldsymbol{\phi}}{\partial \mathbf{x}}\right)\right)\ \forall (\mathbf{x}, \mathbf{u}) \in \mathcal{D} \times \mathcal{U}$, where $\alpha(\frac{\partial \boldsymbol{\phi}}{\partial \mathbf{x}})$ represents the logarithmic matrix norm of the Jacobian matrix $\frac{\partial \boldsymbol{\phi}}{\partial \mathbf{x}}$ of the nonlinear term defined as follows [42]

$$\alpha\left(\frac{\partial \boldsymbol{\phi}}{\partial \mathbf{x}}\right) = \lambda_{\max}\left(\frac{1}{2}\left(\frac{\partial \boldsymbol{\phi}}{\partial \mathbf{x}} + \frac{\partial \boldsymbol{\phi}}{\partial \mathbf{x}}^{\top}\right)\right),$$

and $\lambda_{\max}$ represents the maximum eigenvalue function. We confirm that the nonlinear term $\boldsymbol{\phi}(\mathbf{x}, \mathbf{u})$ is one-sided Lipschitz because the value of the one-sided Lipschitz constant is $\rho = 22.36$ by applying Algorithm 1 described in [25].

REFERENCES

[1] Y. Zhang, Y. Han, C. Wang, J. Wang, and Q. Zhao, "A dynamic threshold method for wind turbine fault detection based on spatial-temporal neural network," J. Renew. Sustain. Energy, vol. 14, no. 5, p. 053304, Sep. 2022.

[2] Q. He, Y. Pang, G. Jiang, and P. Xie, "A spatio-temporal multiscale neural network approach for wind turbine fault diagnosis with imbalanced SCADA data," IEEE Trans. Industr. Inform., vol. 17, no. 10, pp. 6875–6884, Oct. 2021.

[3] F. Deng, M. Jin, C. Liu, M. Liserre, and W. Chen, "Switch open-circuit fault localization strategy for mmcs using sliding-time window based features extraction algorithm," IEEE Transactions on Industrial Electronics, vol. 68, no. 10, pp. 10 193–10 206, 2021.

[4] Y. Han, W. Qi, N. Ding, and Z. Geng, "Short-time wavelet entropy integrating improved lstm for fault diagnosis of modular multilevel converter," IEEE Transactions on Cybernetics, vol. 52, no. 8, pp. 7504–7512, 2022.

[5] S. Zhang, R. Wang, Y. Si, and L. Wang, "An improved convolutional neural network for three-phase inverter fault diagnosis," IEEE Trans. Instrum. Meas., vol. 71, pp. 1–15, Nov. 2022.

[6] Q. Lin, S. Chen, and C.-M. Lin, "Parametric fault diagnosis based on fuzzy cerebellar model neural networks," IEEE Trans. on Power Electron., vol. 66, no. 10, pp. 8104–8115, Oct. 2019.

[7] W.-C. Wang, L. Kou, Q.-D. Yuan, J.-N. Zhou, C. Liu, and G.-W. Cai, "An intelligent fault diagnosis method for open-circuit faults in power-electronics energy conversion system," IEEE Access, vol. 8, pp. 221 039–221 050, Dec. 2020.

[8] F. Wu and J. Zhao, "Current similarity analysis-based open-circuit fault diagnosis for two-level three-phase pwm rectifier," IEEE Trans. on Power Electron., vol. 32, no. 5, pp. 3935–3945, May 2017.

[9] Z. Wu, J. Sun, Y. Song, and J. Zhao, "An open-circuit fault diagnosis method for four-wire t-type three-level rectifier," IEEE Trans. Emerg. Sel. Topics Power Electron., vol. 11, no. 1, pp. 1045–1055, Feb. 2023.

[10] T. Shi, Y. He, T. Wang, J. Tong, B. Li, and F. Deng, "An improved open-switch fault diagnosis technique of a PWM voltage source rectifier based on current distortion," IEEE Trans. on Power Electronics, vol. 34, no. 12, pp. 12 212–12 225, Dec. 2019.

[11] M. Zhang, Z. Zhang, Z. Li, H. Chen, and D. Zhou, "A unified open-circuit-fault diagnosis method for three-level neutral-point-clamped power converters," IEEE Trans. on Power Electronics, vol. 38, no. 3, pp. 3834–3846, Mar. 2023.

[12] D. Zhou, S. Yang, and Y. Tang, "A voltage-based open-circuit fault detection and isolation approach for modular multilevel converters with model-predictive control," IEEE Trans. on Power Electron., vol. 33, no. 11, pp. 9866–9874, Nov. 2018.

[13] H. Yin, Y. Chen, Z. Chen, and M. Li, "Adaptive fast fault location for open-switch faults of voltage source inverter," IEEE Trans. Circuits Syst. I: Regular Papers, vol. 68, no. 9, pp. 3965–3974, Sep. 2021.

[14] W. Zhang, Y. He, and J. Chen, "A robust open-circuit fault diagnosis method for three-level t-type inverters based on phase voltage vector residual under modulation mode switching," IEEE Trans. on Power Electronics, vol. 38, no. 4, pp. 5309–5322, Apr. 2023.

[15] H. Yin, Y. Chen, and Z. Chen, "Observer-based adaptive threshold diagnosis method for open-switch faults of voltage source inverters," Journal of Power Electronics, vol. 20, no. 6, pp. 1573–1582, Aug. 2020.

[16] X. Ding, J. Poon, I. Celanovic, and A. D. Dominguez-Garcia, "Fault detection and isolation filters for three-phase AC-DC power electronics systems," IEEE Trans. Circuits Syst. I: Regular Papers, vol. 60, no. 4, pp. 1038–1051, Apr. 2013.

[17] M. Huang, L. Ding, W. Li, C.-Y. Chen, and Z. Liu, "Distributed observer-based fault-tolerant control for DC microgrids with sensor fault," IEEE Trans. Circuits Syst. I: Regular Papers, vol. 68, no. 4, pp. 1659–1670, Apr. 2021.

[18] T. Wang, L. Liang, S. K. Gurumurthy, F. Ponci, A. Monti, Z. Yang, and R. W. De Doncker, "Model-based fault detection and isolation in dc microgrids using optimal observers," IEEE Trans. Emerg. Sel. Topics Power Electron., vol. 9, no. 5, pp. 5613–5630, Oct. 2021.

[19] N. Pico, S.-H. Park, J. sup Yi, and H. Moon, "Six-wheel robot design methodology and emergency control to prevent

the robot from falling down the stairs," Applied Sciences, vol. 12, no. 9, p. 4403, Apr. 2022. [Online]. Available: https://doi.org/10.3390/app12094403
[20] Z. Wang and Y. Shen, "Residual evaluation based on threshold computation," in Studies in Systems, Decision and Control. Springer Nature Singapore, Oct. 2022, pp. 61–83. [Online]. Available: https://doi.org/10.1007/978-981-19-6706-1_6
[21] S. F. Zarei, H. Mokhtari, and F. Blaabjerg, "Fault detection and protection strategy for islanded inverter-based microgrids," IEEE Trans. Emerg. Sel. Topics Power Electron., vol. 9, no. 1, pp. 472–484, 2021.
[22] A. Bidram, A. Davoudi, and F. L. Lewis, "A multiobjective distributed control framework for islanded ac microgrids," IEEE Trans. on IEEE Trans Industr Inform ., vol. 10, no. 3, pp. 1785–1798, Aug. 2014.
[23] A. Bidram, A. Davoudi, F. L. Lewis, and J. M. Guerrero, "Distributed cooperative secondary control of microgrids using feedback linearization," IEEE Trans. Power Syst., vol. 28, no. 3, pp. 3462–3470, Aug. 2013.
[24] X. Liu, Z. Zou, J. Tang, Z. Wang, and M. Cheng, "Modeling and stability analysis of converter-based power systems," in 2021 IEEE Sustainable Power and Energy Conference (iSPEC). IEEE, Dec. 2021. [Online]. Available: https://doi.org/10.1109/ispec53008.2021.9735799
[25] J. Qi, A. F. Taha, and J. Wang, "Comparing kalman filters and observers for power system dynamic state estimation with model uncertainty and malicious cyber attacks," IEEE Access, vol. 6, pp. 77 155–77 168, Dec. 2018.
[26] M. Abbaszadeh and H. J. Marquez, "Nonlinear observer design for one-sided lipschitz systems," in Proceedings of the 2010 American Control Conference. IEEE, Jun. 2010.
[27] W. Zhang, H. Su, H. Wang, and Z. Han, "Full-order and reduced-order observers for one-sided lipschitz nonlinear systems using riccati equations," Communications in Nonlinear Science and Numerical Simulation, vol. 17, no. 12, pp. 4968–4977, Dec. 2012.
[28] S. A. Nugroho, V. Hoang, M. Radosz, S. Wang, and A. F. Taha, "New insights on one-sided lipschitz and quadratically-inner bounded nonlinear dynamic systems," in 2020 American Control Conf. (ACC), Jul. 2020, pp. 4558–4563.
[29] M. Shoaib, A. Khan, G. Mustafa, S. Gul, O. Khan, and A. Khan, "A framework for observer-based robust fault detection in nonlinear systems with application to synchronous generators in power systems," IEEE Trans. Power Syst., vol. 37, no. 2, pp. 1044–1053, Mar. 2022.
[30] S. Boyd, L. E. Ghaoui, E. Feron, and V. Balakrishnan, Linear Matrix Inequalities in System and Control Theory. SIAM, Jan. 1994.
[31] M. Peet, "Lmi methods in optimal and robust control." [Online]. Available: https://control.asu.edu/Classes/MAE509/509Lecture13.pdf
[32] S. X. Ding, Model-Based Fault Diagnosis Techniques. Springer London, 2013.
[33] E. Ghahremani and I. Kamwa, "Dynamic state estimation in power system by applying the extended kalman filter with unknown inputs to phasor measurements," IEEE Trans. on Power Syst., vol. 26, no. 4, pp. 2556–2566, Nov. 2011.
[34] PowerWorld, "Block Diagrams." [Online]. Available: https://www.powerworld.com/files/Block-Diagrams-18.pdf
[35] NEPLAN, "Exciter Models." [Online]. Available: https://www.neplan.ch/wp-content/uploads/2015/08/Nep_EXCITERS1.pdf
[36] F. Mehmood, P. M. Papadopoulos, L. Hadjidemetriou, A. Charalambous, and M. M. Polycarpou, "Model-based fault diagnosis scheme for current and voltage sensors in grid side converters," IEEE Transactions on Power Electronics, vol. 38, no. 4, pp. 5360–5375, 2023.
[37] S. F. Zarei, M. A. Ghasemi, S. Peyghami, and F. Blaabjerg, "A fault detection scheme for islanded-microgrid with grid-forming inverters," in 2021 6th IEEE Workshop on the Electronic Grid (eGRID), 2021, pp. 01–06.
[38] X. Lu, W. Wang, and J. Ma, "An empirical study of communication infrastructures towards the smart grid: Design, implementation, and evaluation," IEEE Transactions on Smart Grid, vol. 4, no. 1, pp. 170–183, 2013.
[39] K. Elewa, M. Alhasheem, and H. M. Elhelw, "Microgrid applications: Effects of communication systems on secondary control performance," in 2023 5th International Youth Conference on Radio Electronics, Electrical and Power Engineering (REEPE), vol. 5, 2023, pp. 1–6.
[40] F. Dörfler and D. Groß, "Control of low-inertia power systems," Annual Review of Control, Robotics, and Autonomous Systems, vol. 6, no. 1, pp. 415–445, may 2023. [Online]. Available: https://doi.org/10.1146/annurev-control-052622-032657
[41] A. Vijay, S. Doolla, and M. C. Chandorkar, "Unbalance mitigation strategies in microgrids," IET Power Electronics, vol. 13, no. 9, pp. 1687–1710, 2020. [Online]. Available: https://ietresearch.onlinelibrary.wiley.com/doi/abs/10.1049/iet-pel.2019.1080
[42] M. Vidyasagar, Nonlinear Systems Analysis. Society for Industrial and Applied Mathematics, Jan. 2002. [Online]. Available: https://doi.org/10.1137/1.9780898719185

GABRIEL INTRIAGO received the B.E. in Electrical and Computer Engineering from the Escuela Superior Politécnica del Litoral (ESPOL), Ecuador in 2015. He received an M.Sc. in Electrical and Computer Engineering from the University of California Santa Cruz in 2023. He is a Ph.D. student in the Department of Electrical and Computer Engineering at the University of California Santa Cruz. His research interests focus on machine learning, data stream mining, control, optimization, and security with applications to power systems.

YU ZHANG received his B.Eng., M.Sc., and Ph.D. degrees (all with highest honors) in Electrical Engineering from Wuhan University of Technology, Wuhan, China, Shanghai Jiao Tong University, Shanghai, China, University of Minnesota, Minneapolis, MN, USA in 2006, 2010, and 2015 respectively. During the summer of 2014, he was a research intern with ABB US Corporate Research Center, Raleigh, NC. Prof. Zhang received the Huawei Scholarship and the Infineon Scholarship from Shanghai Jiao Tong University (2009), the ECE Dept. Fellowship from the University of Minnesota (2010) and the Student Travel Awards from the SIAM and the IEEE Signal Processing Society (2014). He is an Assistant Professor in the ECE Department of UC Santa Cruz. Before joining UCSC, he was a postdoc at UC Berkeley and Lawrence Berkeley National Laboratory. His research interests span the broad areas of cyber-physical systems, smart power grids, optimization theory, machine learning, and big data analytics.